Comprehensive Modeling of Magnetoinductive Wave Devices for Wireless Power Transfer

Fralett Suárez Sandoval, Ali Moazenzadeh, and Ulrike Wallrabe

***Abstract*—This work presents an analytic model based on the impedance matrix that can predict the transferred energy to a movable receiver device in the near field of a magnetoinductive wave transmitter array. The formulas we present apply to any resonator geometry that can be described as a set of horizontal and vertical segments. The model accurately describes the system efficiency with respect to the operating frequency and to less constraining spatial configurations of the receiver device. The formulated expressions can be easily applied to distinct wireless power transfer system configurations, such as a single pair or an array of resonators, regardless their configuration. We demonstrate that the spatial resolution of the efficiency calculation is limited when only the first coupling order between the receiver and the transmitter array is considered. However, high resolution is possible when first and second coupling orders are included. Additionally, we show that the model foresees the terminating impedance modulation schemes that we applied only after evaluation of data obtained experimentally. These modulation schemes prevent the receiver from standing above a power null resulting from the interaction of forward and backward traveling waves, one of the major challenges in traveling wave based wireless power transfer devices.**

***Index Terms*—Active arrays, energy conversion, frequency modulation, impedance matrix, magnetic resonance, resonators.**

I. Introduction

SEVERAL methods to model magnetoinductive wave devices for wireless power transfer [1]–[6] and other applications [7], [8] can be found in the literature. For example, in former publications [5], [6], we accurately modeled the power transferred to a receiver in the near field of a magnetoinductive wave device using the reflected impedance method. There, we calculated first the net equivalent input impedance presented to a power supply connected to the magnetoinductive wave device. With this impedance, one can easily calculate the output and input powers, defining in this way the efficiency of the system. However, it was possible to predict the system efficiency only when the receiver was perfectly aligned to each cell of the transmitter array because it is time-consuming to obtain a value for the mutual inductance from simulations or measurements. As a result, the models of [2] and [5] predicted a discretized efficiency curve with as many data points as the number of cells. Since the available energy in the near field of the array is a strong function of the spatial configuration of the cells as well as of the movable receiver nearby, the mutual inductance between the receiver with respect to its position and the cells of the array needs to be accurately predicted. Furthermore, when the receiver moves along the transmitter array, there are spatial configurations at which the receiver is coupled to more than one cell of the array at the same time; here, the *Z*-parameter matrix permits to consider all the mutual inductances between the cells of the array and the receiver.

The impedance matrix has been used before [7] to describe the transmission properties of two shifted magnetoinductive waveguides or a one-dimensional (1-D) magnetoinductive wave device [4]. Nevertheless, the estimation of the mutual inductance was found through direct measurement or simulation. In [1], Puccetti *et al.* estimated the mutual inductance between each couple of inductors of their system with good approximation, as well as other electrical parameters of the resonators. This permitted them to describe the transmission parameters for various configurations of the array of resonators. In [2], Stevens showed that the efficiency can be improved along a 1-D magnetoinductive wave array, with the introduction of a termination impedance connected to the last cell. This termination impedance could, for example, match the impedance of the magnetoinductive wave device [9] to avoid the effect of standing waves. However, terminating the device reduces the amount of power that can be transferred to a receiver device because it represents a fixed loss, consequently reducing the system efficiency. In [3], Puccetti *et al.* investigated the effects of the termination impedance on the transmitted power and efficiency as a function of frequency and the position of the receiver. In former publications [5], [6], we proved that it is possible to implement inexpensive circuitry to shift in real time the standing waves along a magnetoinductive wave device to prevent the receiver to stand over a resulting power null. The proposed control scheme was implemented either at the resonance frequency of the device [5] or at a different operating frequency [6]. Nevertheless, these control schemes were based on experimental information retrieved from the induced voltage in a sniffer coil located in the near field of the first resonator of the array. Hence, we could define conditions for this induced voltage that were dependent on the position of the receiver above the array only after experimental characterization. The control schemes proved to be successful

Manuscript received August 2, 2017; revised October 12, 2017; accepted November 21, 2017. Date of publication December 4, 2017; date of current version July 15, 2018. The work of F. Suárez Sandoval was supported in part by the National Council of Science and Technology (CONACyT, Mexico) and in part by the Vector Foundation (Germany). Recommended for publication by Associate Editor Maeve Duffy. *(Corresponding author: Ulrike Wallrabe.)*

The authors are with the Laboratory for Microactuators, Department of Microsystems Engineering, University of Freiburg, Freiburg 79110, Germany (e-mail: fralett.suarez@imtek.uni-freiburg.de; ali.moazenzadeh@imtek.uni-freiburg.de; wallrabe@imtek.uni-freiburg.de).

Color versions of one or more of the figures in this paper are available online at http://ieeexplore.ieee.org.

Digital Object Identifier 10.1109/TPEL.2017.2779606

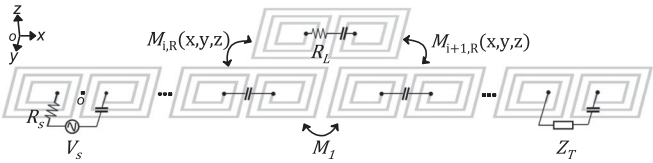

Fig. 1. Exemplary magnetoinductive wave device composed of double-spiral resonators [5] and a receiver of the same kind coupled to them. The resonators on the lower plane are coupled to each other through a mutual inductance M_1. There are intermediate resonators (represented by the ellipsis) not shown for simplicity. The mutual inductance $M_{i,R}(x, y, z)$ between the receiver and the resonators below it is a function of its spatial location with respect to the origin shown.

in adjusting the length of the magnetoinductive wave device in accordance to the position of the receiver. Consequently, the receiver could always be supplied with energy and avoid standing over a resulting null of the forward and backward traveling waves.

The objective of this work is to develop an analytic model that predicts the termination impedance modulation schemes that we applied in [5] and [6] only after experimental characterization. To accomplish this, we use the *Z*-parameter matrix and its inversion to describe the efficiency transferred to a movable receiver in the near field of a magnetoinductive wave device with respect to freer spatial configurations of the receiver and operating frequency. After reading this work, the readers should have gained the necessary tools to design a magnetoinductive wave device of their own with cell geometry and configurations not exclusive to ours. They will also be able to predict the transmitted power to a receiver with less constrained geometries and spatial configurations than those of methods available in the literature. All of the calculated parameters could aid in the optimization of the magnetoinductive wave device for a specific receiver device and power requirements.

In Section II, we present a set of formulas that permits the estimation of the impedance parameters of the resonating cells and of the mutual inductance between any pair of cells in the system. The way the expressions have been formulated allows for its free application to cell geometries that can be described as a set of horizontal and vertical segments, like square, rectangular, S-shape and double-spiral coils of [5]. Section III describes the geometrical and electrical characteristics of the magnetoinductive wave device we used for validating the modeled efficiency. Here, the efficiency predicted for a frequency sweep is compared to experimental results obtained with a vector network analyzer. This section demonstrates that the spatial resolution of the efficiency calculation is limited when only the first coupling order is considered, but high resolution is possible when first and second coupling orders are included. The model also allows for the prediction of parameters like the induced voltage over a sniffer coil that aids in the development of terminating impedance modulation schemes [5], [6].

II. Device Parameters

A 1-D magnetoinductive wave device as shown in Fig. 1 is composed of a finite number of cells (*LC* resonators shown on the lower plane of the figure), which are coupled to each other by a certain mutual inductance. Depending on the cells' configuration and geometry, this coupling could be of the first order M_1, meaning only the nearest neighbor interaction is considered, or of higher order, when the second (or even higher) coupling order is(are) considered. From this figure, we identify that the first cell of the array is connected in series with a power supply V_s, which has a finite output resistance R_s, and that the last cell of the array is connected to a termination impedance Z_T. On the upper plane of the figure, we identify another cell with a load R_L, this cell is a receiver coupled to each resonating cell by a mutual inductance $M_{i,R}(x, y, z)$ that depends on the position in space at which the receiver is. One can describe this system employing the *Z*-parameter matrix (impedance matrix) and its relation to the current and voltage through and across the cells of the array, including those of the receiver, that is

$$\begin{bmatrix} V_1 \\ V_2 \\ \vdots \\ V_n \\ V_R \end{bmatrix} = \begin{bmatrix} Z_{11} & Z_{12} & \dots & Z_{1n} & Z_{1R} \\ Z_{21} & Z_{22} & \dots & Z_{2n} & Z_{2R} \\ \vdots & \vdots & \ddots & \vdots & \vdots \\ Z_{n1} & Z_{n2} & \dots & Z_{nn} & Z_{nR} \\ Z_{R1} & Z_{R2} & \dots & Z_{Rn} & Z_{RR} \end{bmatrix} \begin{bmatrix} I_1 \\ I_2 \\ \vdots \\ I_n \\ I_R \end{bmatrix}. \quad (1)$$

Here, the impedances of the diagonal correspond to each cell's impedance considering any impedance that has been connected to it. For instance, the impedance of the last cell of the array is composed of the series connection of a nonideal inductance and a capacitance (cell impedance) plus the termination impedance Z_T (an additional impedance). The elements right next to the matrix diagonal (except those in the last row and column) are defined by the first coupling order $j\omega M_1$. If higher order interactions are to be considered, impedances such as Z_{13}, for example, become different than zero. The last column and the last row of the impedance matrix indicate how the receiver is coupled to each resonating cell of the array. The receiver impedance is included in the last term of the diagonal Z_{RR}. The voltage vector refers to any external excitation applied to the system. For the system shown in Fig. 1, only the first element is excited, consequently $V_1 = V_s$. The current vector is then the unknown in (1) and can be found with the matrix operation $\boldsymbol{I} = \boldsymbol{Z}^{-1}\boldsymbol{V}$. Once the current vector is known, the system is completely defined. Therefore, one can, for example, express the system efficiency as

$$\eta = 100\frac{\Re(Z_{RR})|I_R|^2}{\Re(Z_{\text{inp}})|I_1|^2} \quad (2)$$

where $Z_{\text{inp}} = V_s/I_1 - R_s$ is the input impedance of the system presented to the power supply and I_R and I_1 are the currents circulating through the receiver and the first cell of the array, respectively. The amount of output power on the receiver will be a function of its position in space and of the operating frequency [6], because parameters such as the impedance of the cells are a function of frequency.

A. Cells' Inductance and Resistance

A well-known approximation for the inductance of planar square, hexagonal, octagonal, and circular spirals has been presented in [10]. However, the formulas there are only valid when the coil geometry in question represents a regular polygon or a

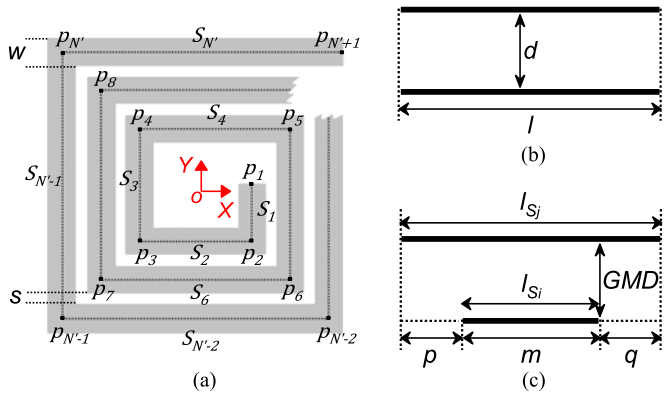

Fig. 2. (a) An exemplary coil geometry whose inductance and resistance need to be determined analytically. The coil is drawn around a center dashed line having a width w. Each segment composed of a pair of vertexes (e.g., p_1 and p_2) is named in increasing order outwards. (b) Two equal infinitesimally thin parallel and straight filaments with a length l and separated by distance d. (c) Two parallel and straight filaments with different lengths and separated by a distance GMD.

circle, which is not the case for a rectangular spiral or the double spirals of [5]. Moreover, authors often rely on simulations to compute the mutual inductance between a pair of coils. Therefore, it will be beneficial to have an accurate and faster method to compute the self-inductance of nonconventional, rectangular-like inductances as well as the mutual inductance between pairs of these. For this reason, here we employ the method proposed in [11] for both self- and mutual inductance calculations.

According to [11], the total inductance of a planar spiral is the sum of each segment's self-inductance and the contribution from the mutual inductance between the segments. Fig. 2(a) shows an exemplary geometry composed of horizontal and vertical segments. Each vertex of the exemplary coil is identified as p_i with coordinates (X_i, Y_i) with respect to the depicted origin.

The length of the segment S_i can be found by

$$l_{S_i} = \sqrt{(X_{i+1} - X_i)^2 + (Y_{i+1} - Y_i)^2}\,. \tag{3}$$

Here, the segments have an increasing subscript number from the most inner segment S_1 outwards. The total number of segments in Fig. 2(a) will be regarded as N'. The self-inductance of each segment, as expressed in [12], is

$$L_{S_i} = \frac{\mu_0}{2\pi} l_{s_i}\left[\ln\left(\frac{2l_{s_i}}{w+t}\right) + 0.5 + \frac{w+t}{3l_{s_i}}\right] \tag{4}$$

where μ_0 is the vacuum magnetic permeability, w is the width of the conductor track, and t is the thickness of the conductor material. Since the direction of the current flow in segments S_2 and S_6 is the same, the mutual inductance between these segments gives a positive contribution to the overall inductance. On the contrary, since the direction of the current flow between segments S_2 and S_4 is in the opposite direction, this mutual inductance will give a negative contribution to the overall inductance of the coil.

To find the positive and negative contributions of the mutual inductance between the segments to the overall inductance, we first take a look at the mutual inductance between two equal infinitesimally thin parallel and straight filaments with a length l and separated at a distance d [see Fig. 2(b)]. The exact mutual inductance of this basic configuration is

$$M = \frac{\mu_0}{2\pi} l\left[\ln\left(\frac{l}{d} + \sqrt{1+\left(\frac{l}{d}\right)^2}\right) - \sqrt{1+\left(\frac{d}{l}\right)^2} + \frac{d}{l}\right] \tag{5}$$

as expressed by [12]. In order to use (5) to find the mutual inductance between the segments S_i and S_j shown in Fig. 2(c), which represent any pair of segments of the coil in Fig. 2(a), one must replace the distance d by the geometric mean distance GMD between the two conductors, which is approximately equal to the distance between the track centers. The exact value of the GMD may be calculated from [11]

$$\mathrm{GMD} = \left(\ln d - \frac{w^2}{12d^2} - \frac{w^4}{60d^4} - \frac{w^6}{168d^6} - \frac{w^8}{360d^8} - \frac{w^{10}}{660d^{10}} + \cdots\right). \tag{6}$$

The geometric mean distance between two conductors is the distance between two infinitesimally thin imaginary filaments whose mutual inductance is equal to the mutual inductance between the two original conductors. This results in

$$M_{\mathrm{GMD}} = \frac{\mu_0}{2\pi} l\left[\ln\left(\frac{l}{\mathrm{GMD}} + \sqrt{1+\left(\frac{l}{\mathrm{GMD}}\right)^2}\right) - \sqrt{1+\left(\frac{\mathrm{GMD}}{l}\right)^2} + \frac{\mathrm{GMD}}{l}\right]. \tag{7}$$

Now, the elementary configuration of the filaments in Fig. 2(b) may be replaced by that in Fig. 2(c). We further identify three auxiliary variables, p, m, and q, related to the existent and absent lengths of the segment on the bottom with respect to the segment on top. When thinking of these elements as any pair of segments from which the exemplary coil in Fig. 2(a) is composed of, the lengths of p and q can become zero. For instance, the pair composed of the segments S_2 and S_4 yields $p = 0$.

The value given by (6) must be distinguished from the self-geometric mean distance of a conductor ($\mathrm{GMD_{self}}$) whose value can be used in (5) instead of d to find the self-inductance of a finite conductor [12]. Useful calculations for the $\mathrm{GMD_{self}}$ of standard geometries can be found in [13]. The $\mathrm{GMD_{self}}$ principle is strictly correct for an infinitely long straight conductor, but is approximately correct for a straight conductor of finite length, as long as the end effects are relatively small (i.e., the conductor cross section is significantly smaller than the conductor length).

The task now is to find the mutual inductance between all possible pairs of segments of the exemplary geometry in Fig. 2(a). To evaluate (7), we need first to calculate the distance between two exemplary segments in question (S_i and S_j). These are $d_{(S_i,S_j)} = |X_i - X_j|$ when the two segments in question are parallel and vertical and $d_{(S_i,S_j)} = |Y_i - Y_j|$ when they are parallel and horizontal. Here, X_i and Y_i represent the abscissa and ordinate of point p_i, respectively. Then, we use (6) to find the GMD between the segments in question. In order to always be able

to represent the pair of segments under examination as the fundamental configuration in Fig. 2(c), we need to identify which of the two segments will have a length m and what the two auxiliary lengths p and q are, this is computed by

$$p = \begin{cases} \min[X_i, X_{i+1}] - \min[X_j, X_{j+1}], & \text{if } l_{S_i} < l_{S_j} \\ \min[X_j, X_{j+1}] - \min[X_i, X_{i+1}], & \text{otherwise} \end{cases}$$

$$q = \begin{cases} \max[X_j, X_{j+1}] - \max[X_i, X_{i+1}], & \text{if } l_{S_i} < l_{S_j} \\ \max[X_i, X_{i+1}] - \max[X_j, X_{j+1}], & \text{otherwise} \end{cases}$$

$$m = \begin{cases} l_{S_i}, & \text{if } l_{S_i} < l_{S_j} \\ l_{S_j}, & \text{otherwise} \end{cases}$$

here, for instance, X_i and X_{i+1} represent the abscissas of points P_i and P_{i+1}, respectively. The mutual inductance between the two segments in Fig. 2(c) is

$$M_{S_i,S_j} = \begin{cases} \pm\frac{1}{2}\Big(M_{(m+p)} + M_{(m+q)} - M_p - M_q\Big), & \text{if } S_i \parallel S_j \\ 0, & \text{if } S_i \perp S_j \end{cases} \tag{8}$$

where $M_{(m+p)}$ and $M_{(m+q)}$ are found by evaluating (5) with l being replaced with $|m+p|$ and $|m+q|$, respectively [11]. Similarly, M_p and M_q are found by evaluating (5) with lengths $|p|$ and $|q|$, respectively. The plus-minus sign in this equation refers to the direction of current flow, if the current through the two segments in question flows in the same direction, $M_{S_i S_j}$ is positive; it is negative when the current flows in opposite directions. Furthermore, when the segments S_i and S_j are perpendicular, the mutual inductance between them is zero.

The mutual inductance contribution to the total inductance of the coil in Fig. 2(a) is found by evaluation of (8) between all pairs of segments and subsequent summation. The total inductance of the exemplary coil is then expressed as

$$L_{\text{tot}} = \sum_{i=1}^{N'} L_{S_i} + 2\sum_{i=1}^{N'-1}\sum_{j=i+1}^{N'} M_{S_i,S_j}\,. \tag{9}$$

The frequency-dependent resistance of the exemplary coil will be then a function of the geometric characteristics of the coil and the skin depth. A study on how the skin effect behaves in conductors with a rectangular cross section was given in [14]. Consequently, we can express the resistance of the coil in Fig. 2(a) as

$$R_{\text{tot}} = \frac{\rho}{wt}\sum_{i=1}^{N'} l_{S_i}\frac{t}{\delta\Big[1-\exp\Big(\frac{-t}{\delta}\Big)\Big]\Big[1+\frac{t}{w}\Big]} \tag{10}$$

where ρ is the resistivity of the conducting material and δ is the skin depth of the material at a given frequency. One must note that this formula does not consider the proximity effect.

B. Mutual Inductance Between Two Coils

The net mutual inductance between two exemplary coils as the ones shown in Fig. 3 can be found by summing the partial mutual inductance between all segment pairs. Fig. 3 shows a configuration of two arbitrary vertical segments S_i and S_j, just as in our previous discussion, there exist the auxiliary variables p, q, and m, which can be determined in the same manner as explained before. The distance between these two parallel and vertical segments can be found by

$$d_{(S_i,S_j)} = \sqrt{(X_i - X_j)^2 + (d_z)^2} \tag{11}$$

where d_z is the axial separation between both coils. The distance between two parallel and horizontal segments will be then given by an expression similar to (11) but with the ordinates instead of the abscissas of points p_i and p_j. The mutual inductance between the two exemplary segments can be found using (8). Then, the net mutual inductance between a pair of coils is

$$M_{\text{tot}} = \sum_{i=1}^{N'}\sum_{j=1}^{N'} M_{S_i,S_j} \tag{12}$$

here the upper limits of summation are determined by the total number of segments from which the coils in question are composed of.

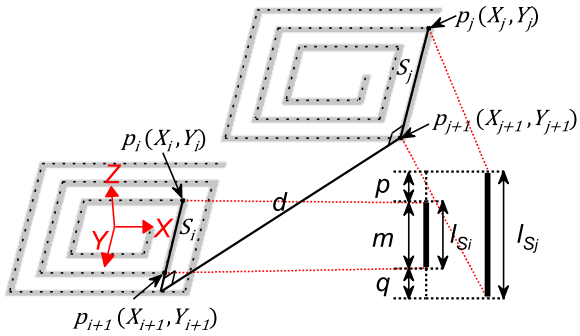

Fig. 3. Auxiliary diagram for the calculation of the mutual inductance between two exemplary coils. The diagram emphasizes on two arbitrary segments S_i and S_j that are separated an axial distance of d_{S_i,S_j}. The total mutual inductance between these two coils is derived by the appropriate summation of the individual mutual inductances between pairs of segments, as expressed by (12).

C. Evaluation of the Generality and Accuracy of the Proposed Method

Because the equations we have just presented use coordinates to describe the coil geometry in question and are independent of the number of turns or the spacing between them, it permits to analyze a new set of possible coil geometries. It also presents the possibility to analyze three-dimensional (3-D) geometries provided that the distance between the segments is calculated in a 3-D space and the geometry can be described as a set of horizontal and vertical segments.

To investigate the accuracy of (9), (10), and (12), in this section we apply them to the geometries shown in Fig. 4. Fig. 4(a) shows a common square spiral with integer number of turns. Fig. 4(b) shows a rectangular spiral with noninteger number of turns and two different spacing between the turns. Fig. 4(c) shows the double-spiral coil proposed in [5]. Finally, Fig. 4(d) shows an S-type coil, in which the winding directions changes

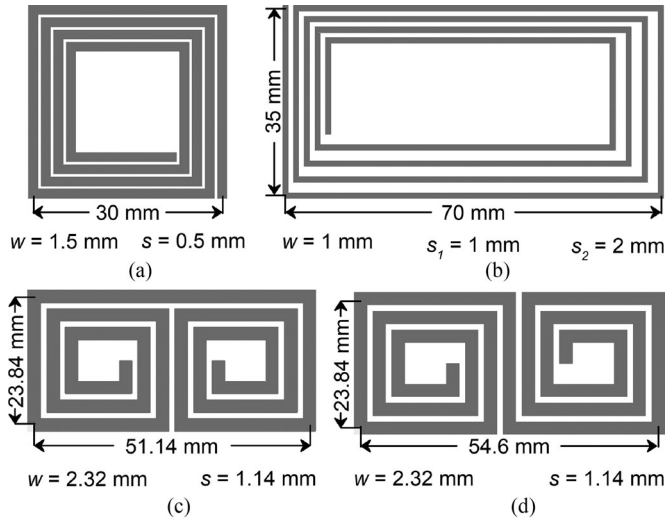

Fig. 4. Distinct geometries used to validate the accuracy of the proposed calculation method for the inductance of a coil and the mutual inductance between pairs of these (see Fig. 5). (a) A square spiral. (b) A rectangular spiral with two different spacings between the conductor tracks and noninteger number of turns. (c) A double-spiral coil of [5]. (d) S-spiral coil inspired by the geometry in (c). The conducting material of all coil geometries is copper with a thickness of 35 μm. Note the width (w) of the copper tracks, the spacing (s) between tracks, and the side lengths in each figure.

TABLE I
CALCULATED AND SIMULATED ELECTRICAL CHARACTERISTICS OF THE COIL GEOMETRIES IN FIG. 4 AT $f = 13.57$ MHz

Coil type		Inductance		Resistance	
		L_{tot} (nH)	Error (%)	R_{tot} (Ω)	Error (%)
(a)	FastHenry	579.6		0.261	
	Calculation	594.8	2.62	0.274	4.98
(b)	FastHenry	1369.5		0.682	
	Calculation	1390.5	1.53	0.78	14.71
(c)	Fasthenry	334.9		0.18	
	Calculation	336.3	0.41	0.186	3.33
(d)	FastHenry	388.2		0.19	
	Calculation	418.8	7.88	0.198	4.21

The coil types (a)–(d) correspond to those shown in Fig. 4(a)–(d), respectively.

from clockwise to anticlockwise. The overall size of the coil geometries, the width of the conductor material (w), and the spacing between the turns (s) are shown in Fig. 4. The conductor material for all of the geometries is assumed to be copper of 35 μm in thickness. Table I shows a comparison between the calculated values of inductance and resistance computed using (9) and (10), respectively, and the values output by a Fasthenry (FastFieldSolvers S.R.L., Italy) simulation with 5 and 13 partitions of the height and width of the conductor [15], respectively.

Table I shows that between the inductance and resistance comparison, the larger error is given by the resistance calculation. Here, one must remember that (10) considers each coil geometry in Fig. 4 as a long and straight conductor with a length given by the summation of the individual lengths of the segments of the coil, i.e., it disregards the proximity effect, whereas FastHenry considers high-frequency effects.

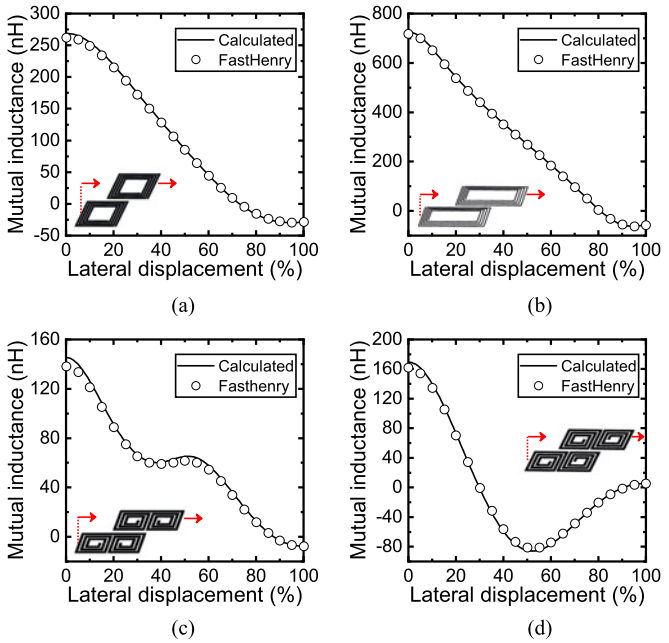

Fig. 5. Comparison between the mutual inductance calculated using (12) and the results of a FastHenry simulation. The evaluated frequency is 13.57 MHz, the axial separation is 5 mm, and the X-axis represents a lateral displacement between both coils as depicted by the inset of the figures. (a) For a pair of the square spiral geometry shown in Fig. 4(a). (b) For a pair of the rectangular geometry shown in Fig. 4(b). For a pair of the double-spiral geometry shown in Fig. 4(c). (d) For a pair of the S-spiral geometry shown in Fig. 4(d).

Fig. 5 shows a comparison made between the mutual inductance computed using (12) and a simulation made with FastHenry for pairs of identical coil geometries as those in Fig. 4. Each pair of coils, as suggested by the insets in Fig. 5, is separated by an illustrative distance of 5 mm in the axial direction. The upper coil moves laterally with respect to the lower one, from a displacement of 0–100% of the length of the coil in the X-direction.

In general, there is a very good agreement between the calculations of the proposed method and the simulation software, which is presented in Table I and Fig. 5. As a comparison, it took FastHenry approximately 30 min to calculate the 21 points shown in Fig. 5(c) for 5 and 13 partitions of the height and width of the conductor [15], respectively, at a frequency of 13.57 MHz. A MATLAB [16] script that computes (12) took only 0.82 s to calculate the hundred data points in the same figure.

Furthermore, since in the upcoming section we will be using the double-spiral coil in Fig. 4(c) for the construction of a transmitter array based on magnetoinductive waves, we characterized several samples of this coil. The samples were professionally fabricated (Wuerth Elektronik, Niedernhall, Germany) with the geometric characteristics shown in Fig. 4. The characterization was done by measuring the forward reflection coefficient with a vector network analyzer (ZVL, Rohde & Schwarz GmbH & Co KG, Germany), we later used this parameter to retrieve the impedance of the coils. The measurement was done for a logarithmic frequency sweep in the range of 1–100 MHz with a resolution bandwidth of 1 kHz. We measured an inductance of 342.9 nH $\pm$ 0.5 nH and a resistance of 270 mΩ $\pm$ 10 mΩ. In

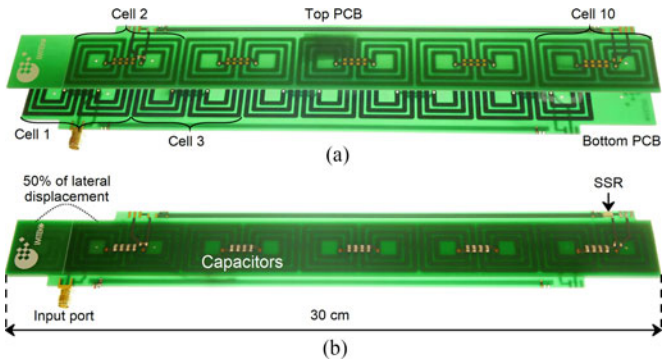

Fig. 6. Magnetoinductive wave device with double-spiral resonating cells. (a) shows the device before being assembled, the top printed circuit board has its five double-spiral coils displaced by half a cell from the bottom PCB. The cells of the array are numbered in increasing order from left to right starting at the bottom PCB, as shown in [5]. (b) After the device is assembled, there exists a total separation of 350 μm between the conductor layers of the boards that face each other. A solid-state relay (SSR) is used for adjusting the length (number of cells) of the device.

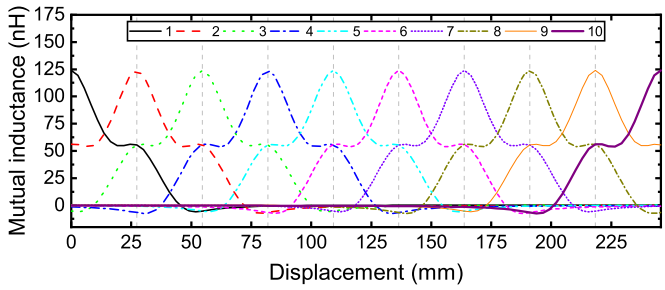

Fig. 7. Mutual inductance between the receiver and the resonating cells of the array. The axial distance between the receiver and odd-numbered cells is 6.15 mm and with even-numbered cells is 5.8 mm [see Fig. 6(a)]. The *X*-axis represents the lateral displacement of the receiver with respect to the array below it. The grid lines are located every time the receiver was in perfect alignment with each cell of the array, this happens every 27.3 mm.

the actual fabricated double-spiral coils that we characterized, there is an increased conductor length needed to bring the coil terminals to the other side of the printed circuit board (PCB) for its subsequent connection to the capacitors, which could account for the difference between the measured inductance and that presented in Table I. The resistance is the parameter that shows the major disagreement between the calculated and measured values, the error sources could be, for example, the fact that (10) does not consider all the high-frequency effects, or the increased resistance due to soldering of the connector needed for characterization, and the increased conductor length discussed above.

III. Model Verification

Now, we shall attempt to apply what we have presented so far on the magnetoinductive wave device presented in Fig. 6. This device is composed of ten double-spiral coils assembled in a brick wall like configuration with 50% of lateral displacement between cells as proposed in [5]. In [6], we demonstrated that due to the good electromagnetic coupling between two double-spiral coils at this lateral displacement, these are preferred over square or rectangular coils for the construction of the array because the attenuation of the traveling wave inside the array diminishes for increasing coupling between the cells. Since the mutual inductance between two coils increases with reducing lateral displacement, as shown in Fig. 5, one must compromise between having a high coupling factor and the manufacturing complexity (PCB layer count) that one is willing to sustain. In [5], we set the maximum PCB layer count as two for the inductive components of the resonating array, plus any other necessary layer for additional components or extra circuitry.

With this lateral displacement, the period between the cells of the array in Fig. 6 is half a cell, which from the dimensions shown in Fig. 4(c) is 27.3 mm. The device is composed of two professionally produced, double-layer PCBs, there exist five cells on the bottom board and five on the top. As observed in the picture, the layers with the conductor tracks meet each other at the center of the device, the outer layers are destined for the capacitive components of resonators as well as other needed components, like the terminating impedance. In this particular device configuration, the isolation between both coil layers is given by two layers of solder-stop with each of 70 μm thickness and a double-sided sticky tape of 175 μm that maintains the boards correctly aligned. Note that the same configuration could have been achieved by a unique PCB of at least three layers if the tracks for the capacitive components are all placed in the same layer. Since the copper layer on each board has a thickness of 35 μm, there exists a total separation of 350 μm between the conductor layers of the boards that face each other. Equation (12) predicts a mutual inductance value of 125.3 nH between two consecutive cells of the array at this axial separation, lateral displacement of 27.3 mm, and a perfect alignment in the *Y*-direction. Also, (12) predicts a mutual inductance of 10.92 nH between nonconsecutive cells (second-order coupling) for a lateral displacement of 54.6 mm, zero axial separation, and a perfect alignment in the *Y*-direction. Whether the second-order coupling needs to be considered will be discussed later.

As mentioned in Section I, a receiver, in this case, of the same geometry as the resonating cells can move above the array. Hence, according to this movement and the receiver geometry, the mutual inductance between the receiver and the magnetoinductive wave device below will change significantly. In order to investigate this change, we evaluate (12) between the receiver and the array. The curves in Fig. 7 show the mutual inductance between the receiver and the cells of the magnetoinductive wave device. The legend identifiers, 1–10, refer to the mutual inductance between the receiver and the cell number corresponding to the identifier. The *X*-axis of this figure represents the lateral displacement of the receiver. We located the grid lines of this figure every time the receiver was in perfect alignment with each cell of the array, this happens every 27.3 mm. If one numbers the array cells as shown in Fig. 6(a), it can be observed from Fig. 7 that the mutual inductance between the receiver and even-numbered cells is slightly higher than between it and odd-numbered cells, this is an effect of the brick wall like configuration of the array. The even-numbered cells are located closer to the receiver for a fixed height of the latter. For the calculations related to this figure, the receiver had an axial separation of 5.8 mm from the even-numbered cells and an axial separation of 6.15 mm from

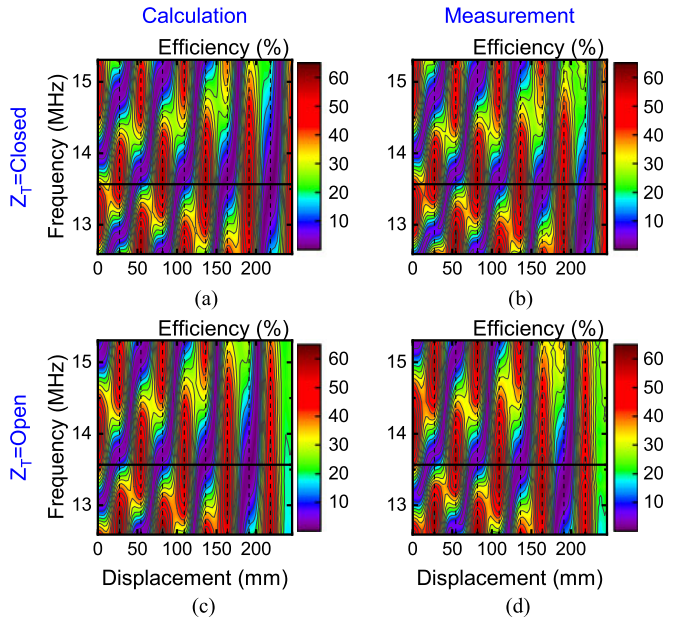

Fig. 8. Comparison between the calculated efficiency resulted after applying (2) for distinct frequency points and what we measured experimentally with a vector network analyzer. The receiver was at an axial separation of 5.8 mm from the uppermost circuit board of the resonating array and had a load of 50 Ω in series. (a) Calculation for a termination impedance set to a close circuit (the array has all of its cells in operation). (b) Measurement corresponding to (a). (c) Calculation for a termination impedance set to an open circuit (the last cell of the array is inactive). (d) Measurement corresponding to (c). The grid lines are located every time the receiver was in perfect alignment with each cell of the array, this happens every 27.3 mm. The wide, black horizontal line marks the design resonance frequency of the transmitter array.

odd-numbered cells. From this figure, it is clear that, for example, at $3 * 27.3$ mm (cell 3) the receiver is considerably coupled to up to three cells of the array (cells 2–4) at the same time.

As we saw in the last section, one must first define (1) completely to calculate the efficiency of the system. We have already calculated the mutual inductances present in the *Z*-parameter matrix. These are the first- and second-order mutual inductances of the magnetoinductive wave device and the mutual inductance between the receiver and the device below. We also defined with (9) and (10) the nonideal inductors, which form the cells of the array. What is still missing is the capacitive part to define the impedances of the *Z*-parameter matrix diagonal. This capacitance is achieved by soldering 400 pF (four capacitors of 100 pF [17] in parallel) in series with each cell. The series configuration of the inductive and capacitive components results in a design resonance frequency of approximately 13.58 MHz. The imaginary part of the impedance of the receiver is the same as the cells of the array, the real part of its impedance is composed of the conductor's resistivity plus an equivalent 50 Ω resistor in series acting as load. This load of 50 Ω in series is considered because port 2 of a vector network analyzer that will be used to characterize the system efficiency is connected in series with the receiver resonator.

Fig. 8(a) and (c) shows the contour plots of the system efficiency as the result of applying (1) for distinct frequencies and receiver positions. Here, the calculation considered that the receiver had the load in series of 50 Ω. The *X*-axis of each subfigure represents the displacement of the receiver with respect to the transmitter array below it. We located the grid lines of this figure every time the receiver was in perfect alignment with each cell of the array, this happens every 27.3 mm. The calculation considered the second-order coupling between the cells of the array, as well as the mutual inductances of the receiver with all the cells of the array. To increase the accuracy of the results, the calculation considered the measured value of the cell's resistance instead of the calculated one. In [5] and [6], we connected the last and the cell before of the array to solid-state relays [18] to change the length of the magnetoinductive wave device according to the position of the receiver on the *X*-axis. However, perfect open or closed circuits cannot be achieved by the nonideal impedances of the relays. In fact, for an LED forward current and voltage of 10 mA and 5 V, respectively, we measured an ON resistance change from 0.6 Ω at 1 MHz to 0.7 Ω at 100 MHz. When the LED is unexcited, instead of representing an infinitely large resistance, the relays have an impedance that changes from 90 to 32 Ω for the same frequency change. Therefore, we have included the measured relay impedances as a series connection to the last two cells of the array in order to perform the calculations of Fig. 8(a) and (c). Fig. 8(a) corresponds to the calculated efficiency when the solid-state relay of the last cell of the array is activated, i.e., a short-circuit termination, similarly, Fig. 8(c) corresponds to an open-circuit termination.

Fig. 8(b) and (d) depicts the efficiency measurement results that were recorded after a full two-port calibration of the vector network analyzer that we mentioned previously. One port of the analyzer is connected to the first cell of the array, as shown in Fig. 1, and the other port serves as a 50 Ω load in series with the receiver. We employed a logarithmic frequency sweep of 801 points in the range of 1–100 MHz with a resolution bandwidth of 1 kHz. Measurements have been performed automatically with a MATLAB [16] script controlling both an XYZ-drive based on an open source g-code parser [19] that will run directly on an Arduino UNO [20] and the analyzer. After recording the *S*-parameters found on one position, MATLAB instructs the XYZ-drive to move to the next position and record the following measurement. Afterward, the efficiency for each position is calculated [21] with

$$\eta = \frac{P_{\text{out}}}{P_{\text{in}}} = \frac{|S_{21}|^2 \left(1 - |\Gamma_L|^2\right)}{\left(1 - |\Gamma_{\text{in}}|^2\right) |1 - S_{22}\Gamma_L|^2} \tag{13}$$

where $\Gamma_L = (Z_L - Z_0)/(Z_L + Z_0)$ is the reflection coefficient looking toward the load Z_L with respect to the reference impedance Z_0, and $\Gamma_{\text{in}} = S_{11} + (S_{11}S_{21}\Gamma_L)/(1 - S_{22}\Gamma_L)$ is the reflection coefficient looking into port one when port two is terminated with Z_L.

Fig. 8 shows a very good agreement between the calculation and the subsequent measurement of the system efficiency. Errors could arise because of the possible differences in the impedance of the cells of the array due to the tolerance of the devices such as the PCB fabrication or the capacitor components. Here, we must remember that the calculation assumed all cells to be perfectly equal; hence, the self-impedances in the

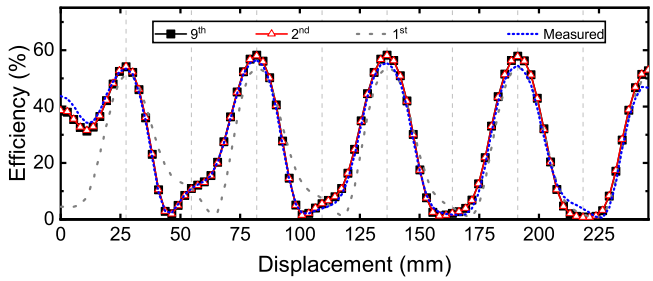

Fig. 9. System efficiency between the input of the system (first cell of the array) and a movable receiver with a load of 50 Ω in series, at an operating frequency of 13.57 MHz and ten operating cells (closed circuit configuration of the solid-state relays). The figure compares the accuracy of the predicted efficiency considering the first-, second-, and ninth-order coupling between the cells of the array and what we measured with a vector network analyzer. The grid lines of this figure are located every time the receiver was in perfect alignment with each cell of the array, this happens every 27.3 mm.

diagonal of the *Z*-matrix are the same for all the cells. It has been proven before that by modulating the terminating impedance of the array according to the receiver position (see [5]) the system efficiency can be enhanced by preventing the receiver to stand over a zero-efficiency point. However, Fig. 8 also shows that for a fixed termination impedance, one can also modulate the excitation frequency to achieve the same goal. For example, consider that for a displacement of 54.6 mm in Fig. 8(a) at the resonance frequency (wide, black horizontal line on each subfigure), there is a low efficiency of about 10%, if one shifts the operating frequency to 12.8 or 14.7 MHz, one could increase the efficiency. Besides, for that displacement, one could also set the termination impedance to an open circuit while maintaining the same operating frequency to achieve the same goal. Modulating the operating frequency, however, requires the power supply of the transmitter array to have a variable frequency, a fact that presents itself as a challenge because budget power supplies are designed to be most efficient at a single operating frequency. In [6], we proved that although one can effectively modulate the termination impedance and obtain higher system efficiency at frequencies other than the resonance frequency, this comes with the penalization of having a magnetoinductive wave device whose impedance is not only real.

Fig. 9 shows what happens with the data given by (2) for an exemplary frequency point when distinct mutual inductances are included in (1). The graphs correspond to a length of ten operating cells, in this case as in Fig. 8(a), the solid-state relays are in the closed configuration. Here, we have considered all the mutual inductances between the receiver and the array. When only the nearest neighbor (first) mutual inductance between the array cells is introduced in (1), one can immediately observe that the calculation differs greatly from the measured data, especially for locations closer to the excitation (displacement of 0 mm) and those at which the receiver is aligned with any cell of the array (displacements given by the grid lines in Fig. 9). If one would introduce in (1) only the first-order mutual inductance and focus only on positions with perfect alignment between the receiver and each cell, one would not be able to distinguish the noticeable disagreement between the calculated and the measured data. If the goal is to better predict the behavior of the system efficiency with respect to freer positions of the receiver, it is necessary to include at least the second-order mutual inductance (second) in (1). As observed in Fig. 9, the measured data agree very well with the calculated ones when the second-order mutual inductance is considered. Furthermore, Fig. 9 shows that when even higher order mutual inductances are considered, the calculated data remain almost unchanged.

IV. Discussion

Now that we have learned how to calculate the necessary parameters to predict the system efficiency with respect to the receiver position and the operating frequency, it is time to explore what sort of information we can obtain from such a formulation. In [5], we predicted the efficiency of the system for a receiver perfectly aligned to each cell of the array using the mutual inductance between the receiver and the cells found through direct measurement and simulation with FastHenry. If we were required to predict the system efficiency for configurations with more spatial freedom, i.e., for more positions above the array, we will find that measuring or simulating the mutual inductance between the receiver and the cells of the array is no longer a viable solution. Fortunately, the formulation presented in Section II for the mutual inductance between the receiver and the cells of the array is applicable to calculate the system efficiency at more arbitrary configurations and locations of the receiver, as shown in Fig. 10. Fig. 10(a) shows what happens with the system efficiency when the receiver is scanned above the working area enclosed by the dashed, black line. The receiver has the same orientation as the cells composing the array and it is providing power to a load of 50 Ω in series with it. The considered operating frequency here is the same as that in Fig. 9, 13.57 MHz. Here, the array has all of its cells in operation, the calculation considered the second-order coupling between the array cells and an axial separation of 5.8 mm between the receiver and the uppermost resonating cells.

Fig. 10(a) shows how the efficiency of the system diminishes when the receiver moves away from a perfect alignment with the cells below it along the *Y*-direction. The power nulls, positions at which the forward and backward traveling waves are in antiphase, are clearly distinguished along the *X*-axis. There is a power null every time the receiver is perfectly aligned with uneven-numbered cells (the ones colored in red in the diagram), i.e., every 54.6 mm.

Fig. 10(b) shows a contour plot for an efficiency analog to that in Fig. 10(a), but with the receiver rotated by 90°. Here, the operating frequency, the number of working cells, and the coupling order are the same as before. The dashed line again encloses the new working area, since now the trajectory of the receiver along the *Y*-axis coincides with its long side, the total displacement along this axis is larger than before. Observe as well that in order to cover the complete length of the array, with this orientation, the receiver travels more distance in the *X*-direction. The highest efficiency measured for this configuration is in general lower than that of the configuration in Fig. 10(a) due to the reduced mutual inductance between perpendicular double-spiral coils. When the receiver is rotated by 90° many

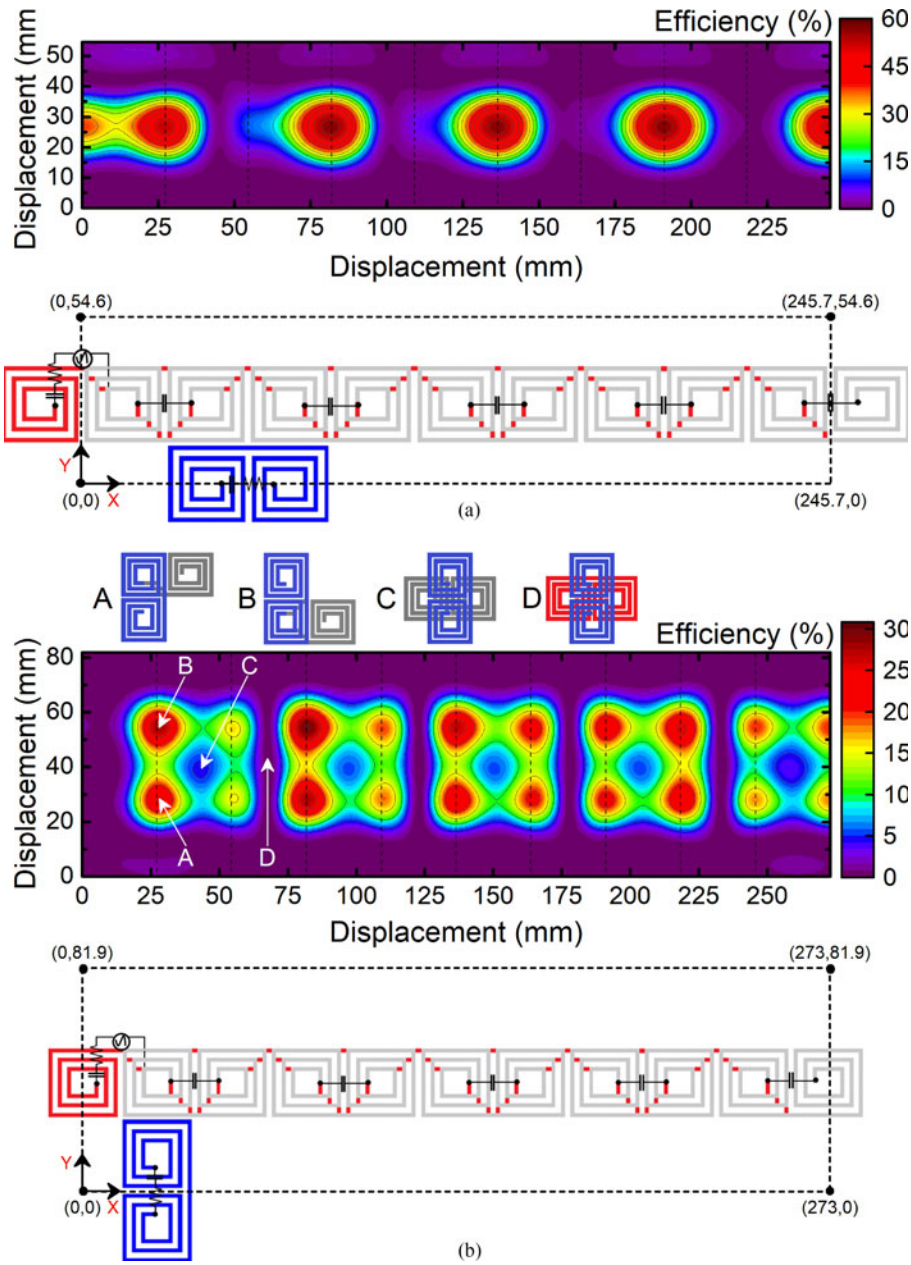

Fig. 10. Calculated contour plots of the system efficiency for an *XY*-scan of the receiver above the resonating array. The receiver was at an axial separation of 5.8 mm from the uppermost circuit board of the resonating array and has a load of 50 Ω in series, the operating frequency is 13.57 MHz. (a) The long side of the receiver cell has the same orientation than the array cells. (b) The long side is oriented perpendicularly to cells of the array. The insets of figure (b) correspond to the locations marked on the contour plot. The diagrams in (a) and (b) show the bottom layer of the array shining through in red, the upper layer in gray, and the receiver device in blue.

of the filaments composing its geometry lay outside the area occupied by the array below it, which increases d, thus yielding a smaller M when evaluating (12). The insets in Fig. 10(b) correspond to the locations marked on the contour plot. When the receiver moves along the Y-axis, every time one spiral of the double-spiral receiver aligns perfectly with one spiral of the double-spiral transmitter below it, the efficiency is high (points similar to A). The efficiency decreases again with further motion along the same axis until increasing once more when the second spiral is aligned in the same manner (points similar to B). Points similar to C correspond to those when the center of the receiver coil is perfectly aligned with the center of a transmitter coil, which is not located on a power null (even-numbered cells). As shown by the inset C, the mutual inductance expected from this configuration is smaller than that of configurations of the insets A or B. The power nulls are also present in Fig. 10(b) (points similar to D) and are located in the same positions of the transmitter array than those in Fig. 10(a), i.e., every time the receiver has its center aligned with the center of an uneven-numbered cell.

In our previous publications [5], [6], we have relied on the direct measurement of a voltage induced across a coil located below the first cell of the array to adjust its length according to the position of the receiver on top. With the formulation we

have presented that one can easily predict this voltage as well in two different ways. One can add an additional cell (cell number 12 in our case) in (1) and fill the impedance matrix accordingly. Taking into account the mutual inductance between this element and the array and the self-impedance of this new element. Consequently, the current through this coil can be found along with the current through the rest of the elements via the impedance matrix inversion, then the voltage across this coil will be

$$V_{sn} = \Re(Z_{sn})|I_{sn}| \tag{14}$$

where the impedance of the sniffer coil is Z_{sn} and the current through it is I_{sn}. The mutual inductance between the sniffer coil and the rest of the system is found with (12). If the magnetoinductive wave device has a configuration in which the second-order coupling can be disregarded, one can also accurately find the voltage across the sniffer coil without the need of adding a new element to (1). Remember that the current through the first element of the array will induce a current through the sniffer coil of the form $I_{sn} = -j\omega M_{sn,1} I_1 / Z_{sn}$, the voltage one will measure across the sniffer coil can be found with (14).

Our previous work has focused on the development of modulation techniques that allow adjusting the length of the magnetoinductive wave device according to the position of the receiver. This was possible, as we mentioned earlier, by monitoring the voltage induced over a sniffer coil located below the first resonating cell of the array. There might be other well-suited parameters that could be monitored to achieve the same goal, like the input impedance Z_{inp}, for example. However, assessment of the feasibility of implementing a modulation technique based on other parameters is beyond the scope of this paper.

Before, the modulation schemes were conceived only after the magnetoinductive wave device was assembled and characterized, because we lacked the estimation of the mutual inductance for different positions of the receiver other than in perfect alignment with the cells of the array. Additionally, we lacked the estimation of V_{sn} with respect to the motion of the receiver. Therefore, we would like to assess the possibility of predicting the modulation schemes, envisioned before, with the tools that we have developed so far. To this end we refer to Fig. 11(a) and (b) that show the terminating impedance modulation that we applied in [5] and [6], respectively. The *Y*-axis shows the number of active cells, note that for Fig. 11(a), the length of the magnetoinductive wave device changes from nine to ten cells, and for Fig. 11(b), one cell is modulated in addition. One must also remember that these modulation schemes did not happen at the same operating frequency of the device. Therefore, it is important to model the behavior of the system with respect to a change in frequency as well. The terminating impedance modulation scheme is based on choosing the length of the magnetoinductive wave device that yields the highest system efficiency after evaluating (2) at every position of the receiver along the *X*-axis, this will be then referred to as the *optimum* modulation scheme. Fig. 11 (a) shows a very good agreement between the optimum modulation scheme developed after experimental characterization (unfilled, red diamonds) and what the modulation would look like with the calculations based on the model we have presented in this work (black solid line). For our calculations, we considered the receiver to have a load in parallel to be consistent to what was reported in [5]. Fig. 11(b) shows three curves, the modulation scheme after our calculation (solid black line), the optimum one after the device characterization (dashed blue line), and that obtained (unfilled, red diamonds) after applying the voltage conditions reported in [6], found also experimentally. The calculations here considered a load of 51 Ω in series with the receiver. Although generally there is a good agreement among the three curves in Fig. 11 (b), some differences exist, for example, at steps 7–12 and 67–73. A possible source of error was already discussed in Section III. Nevertheless, at those particular locations, the calculated modulation scheme still follows one of the other two curves, implying that one would find using the model that we presented here the same operating conditions as those in [6].

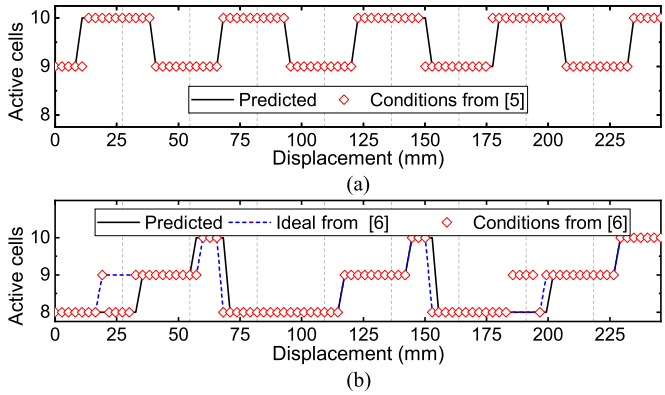

Fig. 11. Comparison between the optimum calculated and measured modulation schemes of (a) [5] and (b) [6]. The optimum modulation is based on choosing the length of the magnetoinductive wave device, between ten or nine operating cells in (a) or ten, nine, or eight operating cells in (b), that will supply energy to the receiver with the highest possible efficiency. The calculated optimum scheme compared using the model of this work is compared to conditions found only after direct measurements of the device. The operating frequency in (a) is 13.65 MHz and in (b) is 11.7 MHz.

V. Conclusion

This work presented an accurate method for calculating the parameters aiding in the description of 1-D magnetoinductive wave devices. The inductive part of the impedance of the resonating cells was estimated by calculating the self-inductance of the segments conforming the coil geometry in question and the contribution of the mutual inductance between the segments to the total inductance of the geometry. An expression for the mutual inductance between any pair of cells of the device, including pairs formed by the receiver and the cells of the array, was also presented. The way the expressions have been formulated allows for their free application to arbitrary geometries that can be described as a set of horizontal and vertical segments. The mutual inductance between a pair of cells of the device was estimated before through simulation or direct measurement once the device was assembled, rendering only very few points along the array at which the efficiency could be compared with the results of the characterization. The availability of a model that can describe input and output

powers in terms of the operating frequency and more spatial configurations of the receiver facilitates tasks such as

1) Formulation of a terminating impedance modulation scheme that prevents the receiver from being above a power null formed by standing waves in the device. Standing waves are one of the major challenges in traveling wave based wireless power transfer devices.
2) Consideration of modulating the transmitter operating frequency with respect to the position of a receiver nearby, as we have seen, the available power for a specific receiver position is a function of the operating frequency as well.
3) Optimization of the system for the power requirements of a specific receiver device.

Using the *Z*-parameter matrix and its inversion allowed us to consider all the relevant mutual inductances between the cells of the resonating array and the receiver, providing an accurate and faster description of the system. A similar approach is envisaged for the description of two-dimensional magnetoinductive wave devices for wireless power transfer and other applications.

ACKNOWLEDGMENT

The authors would like to thank S. M. Torres Delgado from the Laboratory for Simulation, Department of Microsystems Engineering, University of Freiburg, Germany, for valuable discussions and the Laboratory for Electrical Instrumentation, Department of Microsystems Engineering, for access to measurement equipment.

REFERENCES

[1] G. Puccetti, U. Reggiani, and L. Sandrolini, "Experimental analysis of wireless power transmission with spiral resonators," *Energies*, vol. 6, no. 11, pp. 5887–5896, 2013.
[2] C. J. Stevens, "Magnetoinductive waves and wireless power transfer," *IEEE Trans. Power Electron.*, vol. 30, no. 11, pp. 6182–6190, Nov. 2015.
[3] G. Puccetti, C. J. Stevens, U. Reggiani, and L. Sandrolini, "Experimental and numerical investigation of termination impedance effects in wireless power transfer via metamaterial," *Energies*, vol. 8, no. 3, pp. 1882–1895, 2015.
[4] C. J. Stevens, "A magneto-inductive wave wireless power transfer device," *Wireless Power Transf. J.*, vol. 2, no. 1, pp. 51–59, 2015.
[5] F. S. Sandoval, A. Moazenzadeh, S. M. T. Delgado, and U. Wallrabe, "Double-spiral coils and live impedance modulation for efficient wireless power transfer via magnetoinductive waves," in *Proc. IEEE Wireless Power Transf. Conf.*, May 2016, pp. 1–4.
[6] F. S. Sandoval, S. M. T. Delgado, A. Moazenzadeh, and U. Wallrabe, "Nulls-free wireless power transfer with straightforward control of magnetoinductive waves," *IEEE Trans. Microw. Theory Techn.*, vol. 65, no. 4, pp. 1087–1093, Apr. 2017.
[7] A. Radkovskaya *et al.*, "Transmission properties of two shifted magnetoinductive waveguides," *Microw. Opt. Technol. Lett.*, vol. 49, no. 5, pp. 1054–1058, 2007.
[8] C. J. Stevens, C. W. T. Chan, K. Stamatis, and D. J. Edwards, "Magnetic metamaterials as 1-d data transfer channels: An application for magnetoinductive waves," *IEEE Trans. Microw. Theory Techn.*, vol. 58, no. 5, pp. 1248–1256, May 2010.
[9] E. Shamonina and L. Solymar, "Magneto-inductive waves supported by metamaterial elements: Components for a one-dimensional waveguide," *J. Phys. D, Appl. Phys.*, vol. 37, no. 3, pp. 362–367, 2004.
[10] S. S. Mohan, M. del Mar Hershenson, S. P. Boyd, and T. H. Lee, "Simple accurate expressions for planar spiral inductances," *IEEE J. Solid-State Circuits*, vol. 34, no. 10, pp. 1419–1424, Oct. 1999.
[11] H. Greenhouse, "Design of planar rectangular microelectronic inductors," *IEEE Trans. Parts, Hybrids, Packag.*, vol. 10, no. 2, pp. 101–109, Jun. 1974.
[12] F. Grover, *Inductance Calculations: Working Formulas and Tables*, ser. Dover Books on Electrical Engineering Series. New York, NY, USA: Dover, 2009.
[13] J. C. Maxwell, "XXIII, on the geometrical mean distance of two figures on a plane," *Trans. Roy. Soc. Edinburgh*, vol. 26, no. 4, pp. 729–733, 1872.
[14] Y. Eo and W. R. Eisenstadt, "High-speed VLSI interconnect modeling based on s-parameter measurements," *IEEE Trans. Compon., Hybrids Manuf. Technol.*, vol. 16, no. 5, pp. 555–562, Aug. 1993.
[15] M. Kamon, M. J. Tsuk, and J. K. White, "Fasthenry: A multipole-accelerated 3-d inductance extraction program," *IEEE Trans. Microw. Theory Techn.*, vol. 42, no. 9, pp. 1750–1758, Sep. 1994.
[16] "MATLAB Release 2016a," The MathWorks, Inc., Natick, MA, USA.
[17] "Multicomp product number MC0805N101J500CT—SMD multilayer ceramic capacitor." [Online]. Available: http://www.farnell.com/datasheets/1901289.pdf. Accessed on: Jun. 10, 2017.
[18] "World's smallest* SSOP package MOS FET relays with low output capacitance and ON resistance. Product number G3VM-21LR1(TR05)." [Online]. Available: https://www.omron.com/ecb/products/pdf/eng3vm_21lr1.pdf. Accessed on: Jun. 10, 2017.
[19] "GRBL, a free, open source, high performance CNC milling controller." [Online]. Available: https://github.com/gnea/grbl/wiki. Accessed on: Jun. 10, 2017.
[20] "Arduino UNO & Arduino Genuino boards." [Online]. Available: https://www.arduino.cc/en/main/arduinoBoardUno. Accessed on: May 09, 2017.
[21] D. M. Pozar, *Microwave Engineering*. Hoboken, NJ, USA: Wiley, 2012, pp. 558–560.

Fralett Suárez Sandoval was born in Morelia, Michoacan, Mexico, in 1988. She received the B.Eng. degree in electronic engineering from the Morelia Institute of Technology, Morelia, Mexico, in 2011, and the M.Sc. degree in microsystems engineering in 2013 from the University of Freiburg, Freiburg, Germany, where she has been working toward the Ph.D. degree at the Laboratory for Microactuators, Department of Microsystems Engineering, since March 2014.

Her research interests include power electronics and wireless power transmission.

Ali Moazenzadeh was born in Shiraz, Iran, in 1983. He started his academic studies from 2003 in the field of physics. He received the M.Sc. degree in photonics from Shahid Beheshti University, Tehran, Iran, in 2010, and the Ph.D. degree in microsystems engineering for his thesis on "wirebonded microtransformers for power on-chip applications" from the Department of Microsystems Engineering (IMTEK), University of Freiburg, Freiburg, Germany, in 2015.

He is currently a Development Engineer with Voxalytic GmbH, Karlsruhe, Germany, with the goal of commercializing the wirebonded microcoils technology, and in the meanwhile, he is active at IMTEK as a Guest Researcher.

Ulrike Wallrabe received the Ph.D. degree in mechanical engineering of microturbines and micromotors from Karlsruhe University, Karlsruhe, Germany, in 1992.

From 1989 to 2003, she was with the Institute for Microstructure Technology, Forschungszentrum Karlsruhe (today KIT), working on microactuators and optical microelectromechanical systems. She has been a Professor in microactuators with the Department of Microsystems Engineering, University of Freiburg, Freiburg, Germany, since 2003. In 2010, she received an internal fellowship at the Freiburg Institute of Advanced Studies. She has authored or co-authored more than 147 papers in the field of microsystems technology. Her research interest focuses on magnetic microstructures including processes for magnetic materials and microcoils, on adaptive optics, using piezoactuators to tune elastic lenses and mirrors, and on microenergy harvesting.